

Direct measurement of fiber bridging in notched glass-ceramic-matrix composites

Konstantinos G. Dassios^{a)} and Costas Galiotis

University of Patras, Department of Materials Science, Rio University Campus, GR-26504, Greece; and Foundation for Research and Technology Hellas, Institute of Chemical Engineering and High Temperature Chemical Processes, Mechanics of Materials Laboratory, Platani, Platani Patras GR-26504, Greece

(Received 29 September 2005; accepted 17 January 2006)

A novel, high-resolution remote Raman microscope was used for the direct in situ assessment of deformation on bridging fibers in a double-edge-notched SiC-Nicalon reinforced ceramic-glass matrix composite at various stages of monotonic tensile loading. The effect of notch length on the bridging strain profiles obtained by individually probing a large number of fibers across the bridged ligament of the composite was investigated. Bridging strain measurements in the microscale are used to identify the role and sequence of the failure micromechanisms developing within the bridging zone and are compared with their macromechanically derived counterparts. The difference of 25% in failure strain between the as-received fiber and the maximum value obtained on composite-fibers through laser Raman microscopy (LRM), is attributed to the different patterns of fiber failure in composites as compared to the techniques used for fibers characterization such as monofilament and bundle testing in air. This article demonstrates how the LRM-strain data can be utilized to obtain a direct, microscale measure of the interfacial-shear strength of the composite. The obtained interfacial shear strength (ISS) value of 7 MPa compares well with the macromechanically predicted value and offers a much higher precision compared to other experimental techniques.

I. INTRODUCTION

Ceramic matrices reinforced by long continuous fibers constitute a special class of composite materials known as continuous-fibre reinforced ceramic matrix composites (CFCC) with optimal mechanical properties such as strength, damage tolerance, and fracture toughness. CFCCs are much lighter in weight than metals, chemically and electrically inert, and corrosion and oxidation resistant in conventional and high temperatures; they are used as thermal barriers and structural components in applications with high thermomechanical performance demands (aircraft rudders, stabilizers, fins and braking systems; gas turbine blades; space shuttle caps; rocket nozzles, etc).

During the last decade, intense scientific efforts have concentrated on comprehending and analyzing the fracture behavior of CFCCs to improve their design methodologies and lower the high costs associated with their processing routes. Fracture in the vast majority of CFCCs

is related to the formation and propagation of macro-cracks that interact with the interface to give rise to the development of energy-dissipation mechanisms such as interfacial debonding, crack deflection at the interface, crack bridging by intact fibers, and frictional sliding (pull out) of failed fibers. These mechanisms act as internal crack growth inhibitors by consuming a part of the energy applied externally to the CFCC in strain-hardening phenomena, thus decreasing the energy of crack growth through the ceramic matrix. Crack bridging and pull-out are the most prominent of these mechanisms as they can extend to considerable dimensions, often spanning large sections of the composite materials depending on their original size and configuration. Most CFCCs exhibit such large scale bridging (LSB) phenomena, a situation that renders the characterization of their fracture behavior using conventional fracture mechanics (e.g., the R-curve approach), a biased material-extrinsic process dependent on the individual specimen dimensions and configuration.¹ On the other hand, a relation between the local crack opening displacement and the stress exerted on fibers bridging the macro-crack (bridging stress), the bridging law, appears to be independent of the macroscopic geometrical characteristics of the composite and

^{a)}Address all correspondence to this author.

e-mail: kdassios@upatras.gr
DOI: 10.1557/JMR.2006.0132

has been proposed as a material-intrinsic fracture descriptor for CFCCs.²

Bridging laws have been obtained in the past for various composite systems through the use of fracture mechanical approaches such as energy-related methodologies,³ weakest link statistics,⁴⁻⁶ weight function procedures,^{7,8} and other analytical techniques. The shortcoming of fracture mechanics in assessing a microscale phenomenon such as the bridging mechanism is the inherent inability of this approach to assess the role of each phase of the composite independently and to evaluate their mutual interactions. The need to validate the currently available bridging laws by direct measurements of bridging laws in the micro-scale appears, therefore, imperative.

It is well established that spectroscopic techniques such as laser Raman microscopy (LRM) or fluorescence spectroscopy can provide information on the micromechanics of failure for a wide range of single-phase and composite materials. However, very few are the applications of the LRM technique in ceramic materials. Namely, the technique has been used for the in situ measurement of tractional and/or frictional bridging stresses in polycrystalline systems, for example, in a Si_3N_4 polycrystal,⁹ in a zirconia/alumina system,¹⁰ and even in platelet-reinforced composites, for example in an all-alumina composite system.¹¹

In a recent study,¹² the potential of the LRM technique was investigated for the first time in commercial fiber-reinforced ceramic-matrix composites. In the current work, the LRM technique is used for the direct, in situ measurement of bridging strain distribution profiles across the bridged ligaments of SiC_f -reinforced ceramic matrix composite specimens of various notch-to-width ratios loaded monotonically in uniaxial tension. The ability of the technique to individually assess the contribution of the reinforcing phase in the fracture behavior of the composite is demonstrated by separately probing bridging fibers at various stages during mechanical testing using a novel, custom-built variation of the remote Raman microscope¹³ coupled to a servohydraulic mechanical testing frame by direct in situ scanning of the double-edge notched (DEN) specimens' bridged ligaments. The directly measured bridging stress distribution profiles are compared vis-à-vis their macromechanical counterparts that are evaluated following a simple elastic displacement correction approach. The innovative scopes of the study are to investigate the effect of notch length on the magnitude and shape of the directly measured bridging stress profiles and to determine the dependence of the bridging and pull-out mechanisms upon specimen and notch dimensions. To this end, the bridging patterns measured at the micro-scale via the LRM technique are, for the first time here, related to the macromechanical fracture behavior of the composite and to micro-interactions that govern the load transfer mechanisms

active within the composite phases. Additionally, a novel way of measurement of the interfacial-shear strength, based on the directly measured bridging stress, is presented.

II. EXPERIMENTAL PROCEDURES

A. Raman microprobe spectroscopy

Upon excitation, the atomic bonds of a crystalline solid act as dipoles that can vibrate and/or rotate at the frequency of the source but also at different frequencies, characteristic of the nature and strength of the bonds. Analogously, the radiation scattered by a crystal will contain an elastic part having the same frequency as the incident radiation and an inelastic part at different material-specific frequencies. The frequencies of the inelastically scattered radiation are independent of the excitation wavelength and are recorded in the Raman spectrum of a crystalline solid as peaks of various intensities depending on the alteration induced to the crystal-specific polarizability ellipsoid by the incident radiation. The characteristic vibrational and rotational frequencies of a crystal are also affected by changes in interatomic distance.¹⁴ Hence, crystal deformations induce shifts in its characteristic frequencies from their equilibrium values. Due to the anharmonicity of the interatomic potential well, a change in interatomic distance, caused for example by a strain field, will provoke an analogous shift in characteristic frequency. The LRM technique relies on the observation that mechanically induced shifts in characteristic frequencies are mathematically related to the deformation of the crystalline material, usually through a simple linear expression.^{15,16} Crystalline materials, such as most ceramic fibers, directly transfer the external deformations to the atomic bonds, serving in this regard as ideal spectromechanical sensors. In practice, the methodology followed for the determination of local deformation on a macroscopically loaded fiber via the LRM technique involves, initially, the determination of the scatterer-specific Raman calibration curve and that is subsequently used to convert the wavenumber shifts of fibers in the composite into strain.

The experimental setup used for the in situ collection of Raman spectra on mechanically loaded fibers has been presented in a previous work.¹⁷ In brief, the system consists of a compact remote Raman microscope (Model custom-built by Dilor/Jobin Yvon SAS, Lille, France) with an integrated miniature diode-pumped solid-state laser source transmitting a monochromatic radiation of a wavelength of 514.5 nm. A selection of objective lenses provide the microscope with magnification power options of 4× to 80× and the ability to serve both as a damage observation tool and a high resolution probe. A micro-translational stage positioned in front of a servo-hydraulic testing frame (Model 858 Tabletop, MTS Systems Corp., Eden Prairie, MN) is used to travel the Remote Raman

microscope (ReRaM) in discrete steps of $1.2\ \mu\text{m}$ in three dimensions and facilitate focusing of the laser beam on distinct fibers during mechanical testing. The spectroscopic signal is transferred to a remote spectrometer (Model 1000M Single Monochromator, SPEX, SPEX Industries Inc., Edison, NJ) using polarization-preserving fiber optics where it is analyzed in terms of Raman wave number shifts. The polarization of the excitation radiation was set parallel to the expected orientation of bridging fibers, as crystal vibrations are more intense parallel to the fiber axis,¹⁸ thus providing sharper spectra.

B. Materials and testing procedures

The composite material under investigation, originally expected as thermal barrier of the European space shuttle (Ariane) is a continuous-fiber reinforced glass-ceramic matrix cross-ply laminate processed by European Aeronautic Defense and Space Company (EADS), France. The brittle matrix consists of a sol-gel-derived mixture of metal oxides, namely MgO , Al_2O_3 , SiO_2 , and Li_2O . The embedded SiC-Nicalon fibers (Grade Nicalon NLM202, Nippon Carbon Co. Ltd., Tokyo, Japan) are the pyrolytic product of a polymeric polycarbosilane. Laminated plates of a thickness of 2 mm have been obtained through hot-pressing of 8 unidirectional infiltrated plies of aligned fiber bundles stacked in a symmetric $[0/90]_{2s}$ orientation. The main properties of the composite, as reported by EADS, are presented in Table I.

TABLE I. Main properties of the SiC/MAS-L composite.^{26,29}

Property	Value
Chemical composition of matrix (% b.w.)	
MgO	0.5
Al_2O_3	1.0
SiO_2	4.0
Li_2O	0.5
Chemical composition of fibers (% b.w.)	
Si	56.6
C	31.7
O	11.7
Young's modulus of matrix (GPa)	75
Young's modulus of fibers (GPa)	220
Thermal expansion coefficient of matrix ($10^{-6}/^\circ\text{C}$)	2.1
Thermal expansion coefficient of fibers ($10^{-6}/^\circ\text{C}$)	
Longitudinal	3.9
Transverse	2.9
Fiber diameter (μm)	12–14
Fiber volume fraction (–)	0.33
Apparent density (g/cm^3)	2.50
Ply thickness (mm)	0.25
Longitudinal Young's modulus (GPa)	123
Tensile strength (GPa)	400
Poisson's coefficient (–)	0.23
Hot-press temperature ($^\circ\text{C}$)	1300
Thermal expansion coefficient (20–1000 $^\circ\text{C}$) ($10^{-6}/^\circ\text{C}$)	
Parallel to fibers	3.4
Perpendicular to fibers	1.7

The composite plates were processed in a computer numerical control (CNC) vertical machining center using a $300\ \mu\text{m}$ thick diamond wafering blade (Model 5 LC Diamond Series, Buehler Co. Ltd., Lake Bluff, IL) for the preparation of double-edge notched specimens. This specimen configuration offers the advantage that damage is localized within the notched ligament of the material. The specimens were machined under the condition that the bridging phenomenon should be optically accessible on the specimen outer surface; thus the orientation of the fibers in the external plies of the material was set to coincide with the loading direction. A schematic illustration of the geometrical characteristics of the specimens is presented in Fig. 1, and the dimensions of specimens used in this study are given in Table II.

Nine DEN specimens of notch-to-width ratios of 0.4, 0.5, and 0.6 were tested in displacement-controlled monotonic tension at an MTS servohydraulic frame equipped with a 25 kN load cell. A constant cross-head displacement rate of $10\ \mu\text{m}/\text{min}$ was used for all specimens, and an axial extensometer (Model 632.24F-50, MTS Systems Corp.) of a gauge length of 25 mm equipped with knife edges was used to measure strain directly on the material.

The LRM technique was used on three of the DEN specimens, one for each of the notch-to-width ratios. From the onset of the experiment, a $4\times$ magnification lens was used to observe optically the surface of the specimen notched ligament where all damage was expected to concentrate. The recorded fracture sequence commences with the formation of matrix microcracks in both notch roots and the appearance of the bridging zone. With further loading, microcracks propagate within the matrix toward the facing notch until a critical crack density is established where the paths of opposite

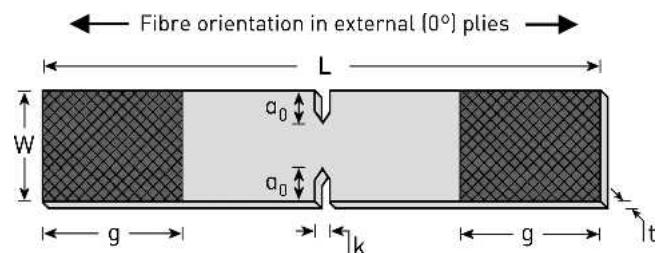


FIG. 1. Definition of geometrical characteristics of DEN specimens.

TABLE II. Dimensions of tested specimens.

Dimension	Value (mm)
Width, W	12.0
Thickness, t	2.0
Length, L	120.0
Gripped length, g	30.0
Notch width, k	0.3
Notch-to-width ratio, $2a_0/W$	0.4, 0.5, 0.6

microcracks merge to form a dominant, fully developed macrocrack spanning the whole notched ligament of the specimen. Upon the formation of a fully developed macrocrack, the remaining microcracks do not propagate further. The formation of the dominant macro-crack defines also the fully developed bridging zone where (bridging) fibers stretch and fail to give rise to the pull-out effect.¹² Due to the high brittleness of the glass-ceramic matrix, crack propagation in the particular composite is a very rapid process, and the macro-crack and bridging zone become fully developed almost instantly after first matrix cracking.

The bridging and pull-out mechanisms of the specific composite are of particularly large scale, visible also to the naked eye, as demonstrated in Fig. 2(a). Once the dominant macro-crack was developed, the crosshead displacement was temporarily paused, and the magnification of the objective lens was switched to 50× to allow for LRM-probe scanning of the bridged ligament [Fig. 2(b)]. At that magnification level, the laser spot attains a diameter of ~4.5 μm, which corresponds to approximately 35% of the scattering fiber diameter. A minimum of 100 fibers were individually probed at each interruption stage in representative, equally distributed locations across the bridging zone. Additionally, a minimum of three spectra were collected on different positions along the length of each fiber to assess spectrum repeatability along the fiber.

C. Raman signal of SiC Nicalon fiber

The crystal structure of the silicon carbide NLM202 fiber consists of free carbon nanoprecipitates and nanocrystalline β-SiC grains forming an amorphous oxycarbide of chemical formula $\text{SiC}_{1.15}\text{O}_{0.85}$.^{19,20} While oxygen is introduced during fiber curing,²¹ the existence of excess carbon relative to silicon (attributed to the high C-to-Si ratio in the polycarbosilane precursor) is responsible for the appearance of the prominent 1350 and 1675 cm^{-1} bands in the Raman spectrum of the SiC NLM202 fiber. These bands correspond, respectively, to

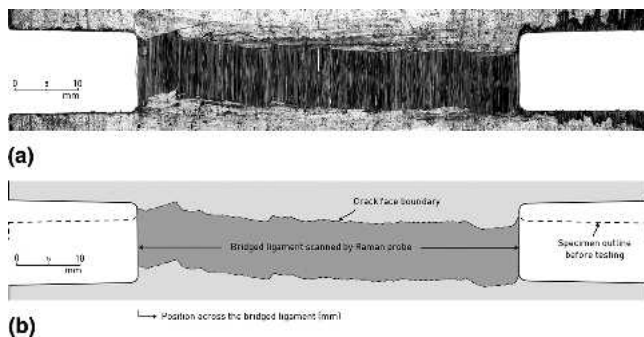


FIG. 2. Post-mortem depiction of the bridged ligament of a DEN specimen with $W = 10.0$ mm and $2\alpha_0/W = 0.4$: (a) Low-magnification optical microscope image and (b) schematic overview of the fracture extent as compared to initial specimen condition.

the A_{1g} breathing mode and E_{2g} stretching mode of the C–C bond in the graphite crystal (Fig. 3).

The high process temperature of the composite (Table I) has caused the graphitization of embedded fibers, thus altering their crystallinity and mechanical properties.²² This effect was confirmed by comparison of the Raman spectra of as-received NLM202 fibers and fibers extracted from the composite using a wet dilution technique in an alcohol solution. As shown in Fig. 3, the A_{1g} and E_{2g} bands of the extracted fibers are much more well-defined than those in the as-received fiber spectrum, indicating a more robust crystal structure in the primer case. To obtain a Raman calibration curve characteristic of the exact crystalline and mechanical properties of the target scatterer, the calibration procedure was performed on fibers extracted from composite instead of the as-received fibers.

The Raman spectrum of the NLM202 fiber is very sensitive to incident radiation. High laser powers and exposure times can induce undesirable shifts in the scattered signal due to local thermal energy accumulation effects on the scatterer's surface.¹⁷ Following a parametric study of the effect of the two parameters on the A_{1g}

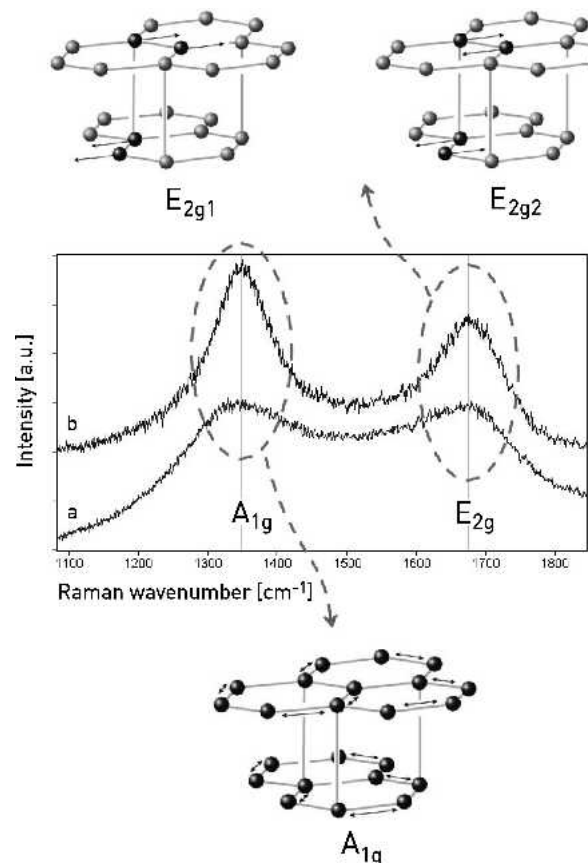


FIG. 3. A_{1g} and E_{2g} vibrational modes of graphite and the corresponding Raman spectra of the NLM202 fiber in (a) the as-received condition and (b) embedded in the composite.

band position, the optimal combination of laser power and exposure time was found to be 2.85 mW and 20 s, respectively. The standard deviation of the A_{1g} band position under the established exposure conditions was 0.17 cm^{-1} .

The Raman calibration procedure was determined by loading individual fibers extracted from the composite in incremental tensile displacement using the conventional “paper window” tab method (10 mm gauge length). The monofilaments were tested on a miniature materials tester (Minimat 2000, Rheometric Scientific, Surrey, UK), and the position of the A_{1g} band as a function of fiber strain was optimally approximated by a linear expression with a slope of $7.49 \text{ cm}^{-1}/\text{strain}\%$. This value served in the conversion of A_{1g} band shifts in the spectra of bridging fibers to bridging strain and subsequently to stress through the fibers’ Young’s modulus.

D. Macromechanical bridging law

In displacement-controlled testing, the total displacement of a DEN specimen is the sum of a linear contribution corresponding to reversible deformation and a nonlinear contribution corresponding to the irreversible mechanism of fracture. In CFCCs, the latter contribution is, in turn, directly associated with crack opening and the corresponding formation of the bridging zone. Thus, once the elastic displacement is subtracted from the total displacement of the system, a direct relation can be drawn between the crack opening and the load carried by fibers within the bridging zone, i.e., the bridging load. The crack opening displacement, denoted e , can be evaluated at each loading instance from the experimental load–displacement (F, d) pair values, through¹²:

$$e(d) = d - C_0 F(d) \quad , \quad (1)$$

where C_0 is the compliance of the composite within the elastic regime. Following Eq. (1), the original load–displacement [$F(d)$] behavior of the composite is converted into bridging load–crack opening displacement behavior [$F_{br}(e)$]. Additionally, the nominal bridging stress as a function of crack opening displacement, $\sigma_{br}(e)$, i.e., the macromechanical bridging law of the composite, is found through

$$\sigma_{br}(e) = \frac{F_{br}(e)}{t(W - 2\alpha_0)} \quad , \quad (2)$$

where t and W are the specimen thickness and width, respectively, whereas α_0 is the length of the initial notch.

III. RESULTS

A. Macromechanical bridging stresses

The bridging laws, derived from the corresponding recorded load–displacement behavior by application of

the elastic displacement correction [Eq. (2)], are presented in Fig. 4 for three DEN specimens of different initial notch-to-width ratios. It is observed from Figs. 4(a)–4(c) that the maximum bridging stress attained by the composite ($\sim 150 \text{ MPa}$), is independent of the notch length, an effect compatible with the notch-insensitive nature of CFCCs. In contrast, the shape of the bridging law appears to depend on this parameter with longer notches causing a sharper decrease in stress after the attainment of the maximum value; a behavior corresponding to a more massive fiber failure scenario.

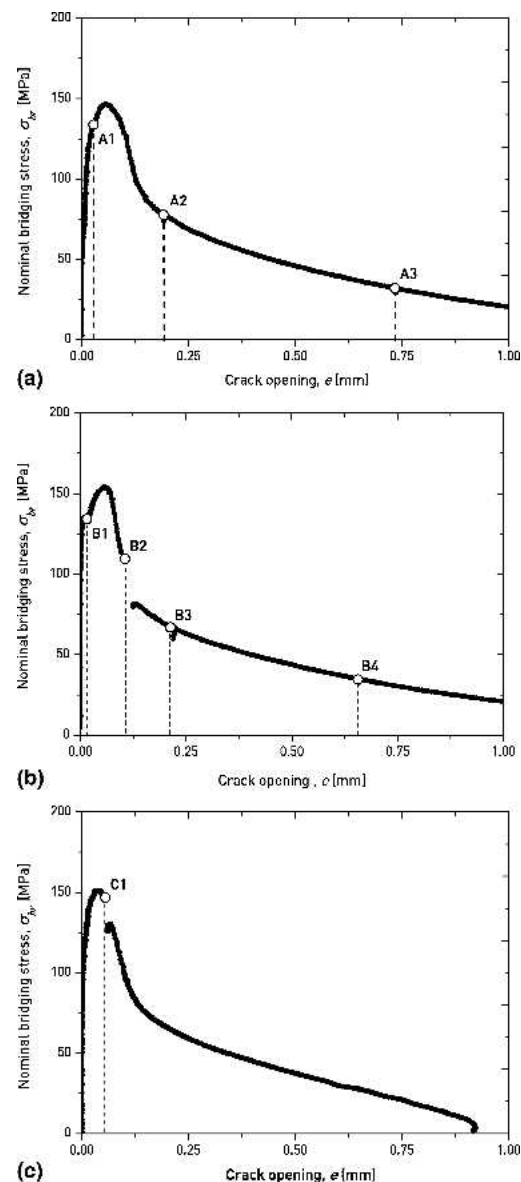


FIG. 4. Macromechanically obtained bridging laws for 3 specimens with different notch-to-width ratios. The dashed lines demonstrate the loci of LRM measurements across the bridging zone. (a) Specimen A, $t = 2.0 \text{ mm}$, $W = 12.0 \text{ mm}$, $2\alpha_0/W = 0.4$; (b) Specimen B, $t = 2.0 \text{ mm}$, $W = 12.0 \text{ mm}$, $2\alpha_0/W = 0.5$; and (c) Specimen C, $t = 2.0 \text{ mm}$, $W = 12.0 \text{ mm}$, $2\alpha_0/W = 0.6$.

Given the fact that both width and thickness are constant for all specimens, the observed behavior can be attributed to the smaller number of fibers available to evenly share the global load within the ligaments of deeper-notched specimens.

The experimental data of Fig. 4 exhibit transient load relaxations in certain positions. These positions, also indicated by dashed vertical lines, correspond to the instances of “freezing” the input deformation to perform LRM scanning of the bridging zone. The observed load drops are larger at sensitive fracture instances such as at the end of the fiber failure regime where a small number of fibers remain intact [LRM-Acquisition Stage B2 in Fig. 4(b)] or after the maximum load is taken up by the composite [LRM-AS C1 in Fig. 4(c)]. On the other hand, load relaxation is significantly less at less-critical fracture instances such as the onset of fiber failure [LRM-AS B1 in Fig. 4(b)] where the integrity of the material remains practically unaffected or during pull-out-dominated fracture (LRM-AS A2, A3, B3, B4). The latter observation leads to the conclusion that pull-out is a much more robust toughening mechanism for the specific composite than bridging. This effect is due to the different nature of the two mechanisms, pull-out being a friction process during sliding of the fiber surface along the debonded interface, while bridging is an instability-intolerant mechanism of global load sharing among a large number of fibers acting independently, at the microscale.

B. Direct LRM-based measurement of local bridging strain

The Raman spectra collected on bridging fibers were analyzed in terms of wave number shifts of the A_{1g} band from the stress-free position. The latter was calculated as the mean A_{1g} band position in a total of 50 spectra obtained on tips of completely pulled-out fibers on completion of the composite testing. The standard deviation of these measurements was calculated as 0.38 cm^{-1} . The observed shifts were converted to equivalent fiber strain through the slope of the established Raman calibration curve ($7.49 \text{ cm}^{-1}/\%$ strain).

The bridging strain, as measured directly on fibers at each LRM-acquisition stage, is plotted versus normalized position across the bridged ligaments (NPBL) in Fig. 5 for specimen A of initial notch-to-width ratio of 0.4. The loading condition at which each acquisition stage was performed is noted with an open cycle in the corresponding load–displacement curves in the left subset of Fig. 5. At each acquisition stage (A1, A2, A3), the mean values of repetitive measurements on each fiber are plotted as solid cycle symbols along with the standard deviation appearing as error bars.

While strain is distributed, within experimental error, uniformly among the bridging fibers in the largest part of the material, there is a marked strain-relaxation in the vicinity of the notch roots. This relaxation phenomenon in bridging strain may be attributed to strain magnification gradients developing in the matrix material around

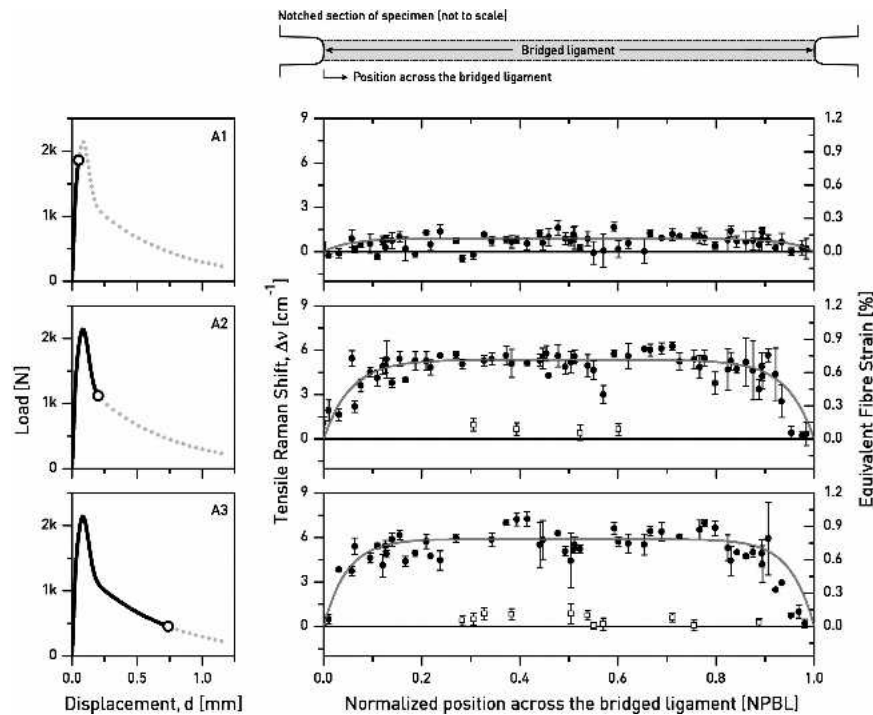


FIG. 5. Directly measured bridging strain distribution profiles for specimen A with $t = 2.0 \text{ mm}$, $W = 12 \text{ mm}$, and $2\alpha_0/W = 0.4$.

the notches. These local gradients, of decreasing magnitude with increasing distance from the notch tip, induce premature fiber failure around the notches and lower the local load-bearing potential of the bridging zone. As can be deduced by examination of Fig. 5, this strain-relaxation phenomenon spans a length of 0.1 NPBL on either side of notch root, which is independent of the level of loading.

The experimental data of bridging strain for each specimen and each acquisition stage are fitted with a step-wise exponential function of the form:

$$y = \begin{cases} \alpha_1 \exp(-b_1 x) & 0 \leq x < 0.5 \\ \alpha_2 \exp[b_2(x - 1)] & 0.5 \leq x < 1 \end{cases}, \quad (3)$$

where y represents the Raman shift $\Delta\nu$, x represents the normalized position across the bridged ligament, and α_i and b_i are the regression parameters. The particular function type was chosen among a number of complex regression functions for its simplicity and possible physical meaning in simulating a strain relaxation phenomenon around a discontinuity.²³ The following fitting procedure was pursued for simulating the bridging profile:

(i) The plateau value of $y(0.5^-)$ should coincide with the plateau value of $y(0.5^+)$. If the output values of the regression parameters α_1 and α_2 are not equal, the mean value of α_1 and α_2 is selected.

(ii) The strain relaxation gradient should be symmetric with respect to distance from the notch root. If the output values of the regression parameters b_1 and b_2 are not equal, the value of b_i associated with the smallest standard error is selected.

The resultant bridging profiles for all specimens and acquisition stages are summarized in Fig. 6. This figure demonstrates that strain relaxation appears to concentrate within ~ 0.1 NPBL from each notch, independent of notch length. This observation can be rationalized upon the much smaller length scale over which the strain magnification

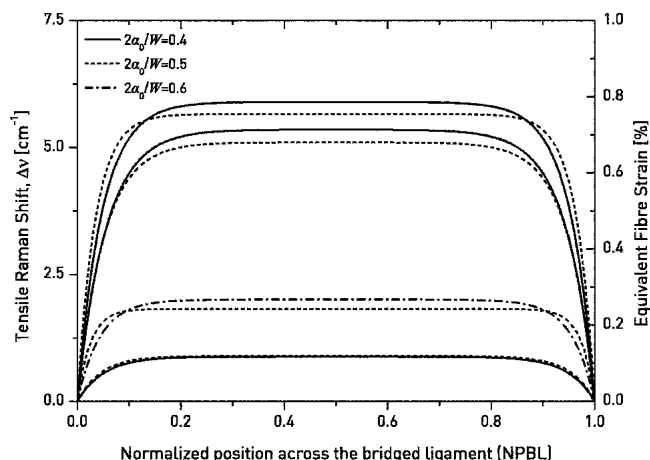


FIG. 6. Regressions to the experimental bridging strain profiles of 3 specimens of different notch lengths.

mechanism acts compared to specimen width. In other words, the specimen width is large enough to allow the strain gradients to build independently in both notch roots as in the far-field case of a plate of infinite width.

IV. DISCUSSION

A. Intra-fiber variations

The zero-strain data drawn as open square symbols in Fig. 5 correspond to load-free fibers that have failed either within the crack flanks or in irregularly short lengths within the matrix and have pulled out completely. The increasing number of zero-strain fibers in successive acquisition stages within the same specimen, as for example in Figs. 5(b) and 5(c), indicates the progressive disengagement of an increasing number of pull-out fibers from the matrix material.

The scatter of experimental data in Fig. 5 and in the bridging profiles of specimens of initial notch-to-width ratios of 0.5 and 0.6 is characteristic of the complexity of the mechanisms developing during composite fracture. Although strain distribution profiles across the specimen ligaments are explicitly determined, especially in advanced fracture instances, the variation between individual local values manifests the effects of fiber inhomogeneity, stress singularities, and volume micro-irregularities that govern the overall composite behavior; effects that are usually inaccessible through macromechanics. On the other hand, the strain is distributed uniformly along the fiber length, with the standard deviation of A_{1g} band in spectra collected on different positions of the same fiber falling within the scatter range of the stress-free measurements.

B. Micromechanics of failure within the bridging zone

The maximum (plateau) values of local bridging strains are shown for the three specimens of different notch length in Fig. 7 as a function of crack opening e . In this graph, the experimental data are drawn as open symbols whereas the error bars represent the standard error of the regression for each acquisition step. As seen in Fig. 7, bridging strain exhibits a saturation behavior, reaching a value of approximately 0.75% at crack openings of 0.2 mm that is never exceeded with further loading.

To explain the observed behavior, it is essential that the fracture procedure of the composite material under investigation is well understood. The fracture sequence of externally loaded brittle ceramic-matrix composites is triggered by the appearance of matrix microcracks originating usually from porosity imperfections, voids, enclosures, or flaws in the matrix. The propagating cracks eventually approach the vicinity of fibers where they deflect along the interface (which is weaker than the matrix), causing the local rupture of the complex bonds

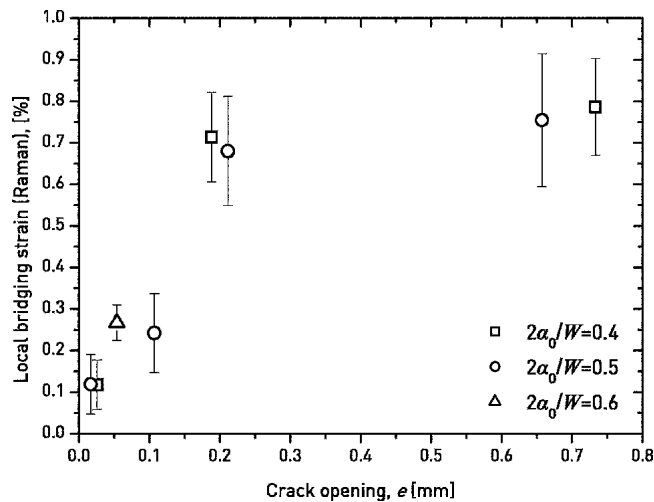


FIG. 7. Three dimensional projection of the change in fiber strain as a function of crack opening and normalized position across the bridged ligament. Directly measured local bridging strain for specimens with different notch lengths as a function of crack opening.

between matrix and fiber (debonding; see also Fig. 8, process 1). Interfacial debonding endures until the energy consumed in the specific damage mechanism balances the work required for further crack growth. In other words, once the externally applied energy has caused enough damage to the interface around the fiber for the mechanism of crack growth to become energetically more preferable, the crack will propagate further in front of the debonded fiber-matrix interface. The phenomenon evolves self-similarly each time the crack front encounters new fibers. Behind the crack front, bridging fibers stretch freely along the separating crack faces (exposed length) but also along the debond length where stretching is restricted by friction due to sliding of the fiber's surface along the debonded interface. Due to the weaker nature of the interface compared to that of the matrix, the debond length is usually much larger than the instantaneous separation of the crack faces (crack opening). For example, the mean pull-out length for the composite in this study is of the order of 0.7 mm^{12} while crack opening is approximately 0.05 mm at the onset of fiber failure. Thus, as loading continues, the probability of a fiber failing along the debond length is much higher than the probability of it failing within the crack flanks. Fibers that have failed within the debond length slide across the interface, giving rise to the appearance of the pull-out mechanism. It is expected that the maximum load on a fiber due to frictional sliding along the debonded interface can never exceed the load capacity of an intact fiber. In other words, the pull-out mechanism can only produce forces equal or less in magnitude than those produced by the bridging mechanism.

In Fig. 7, the experimental data corresponding to crack openings smaller than 0.2 mm originate from acquisition stages for which most of the probed fibers are intact and

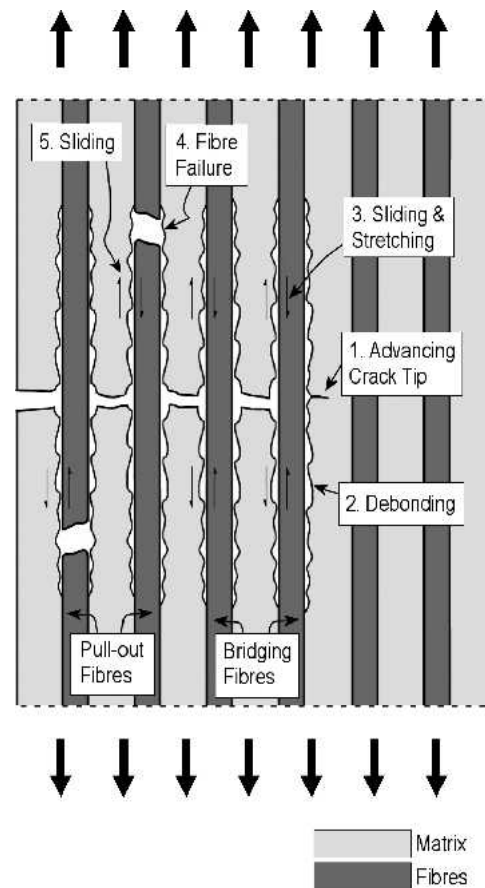


FIG. 8. Sequence of processes during the fracture procedure of a brittle matrix continuous-fiber reinforced composite (not to scale).

the local values correspond mostly to pure bridging strain. On the other hand, the last two data points in Fig. 7, at crack openings of 0.75 mm , originate from acquisition stages for which all of the probed fibers have failed and are undergoing pull-out. Thus, the strain on these fibers cannot exceed the maximum strain established on intact fibers up to crack openings of 0.2 mm . Based on the above remarks and by observation of Fig. 4, it can be concluded that the fracture behavior of the material becomes dominated by the pull-out mechanism at approximately 0.2 mm crack opening for all specimens.

C. Fiber strength and failure pattern in composite

It is interesting to compare the plateau value of the LRM-measured fiber strain, $\sim 0.75\%$, to the failure strain of the as-received SiC Nicalon fiber. For the continuous-fiber reinforced composite under investigation, the relevant gauge length of fibers is assumed equal to the loaded length of the specimen, 60 mm , calculated by subtracting the gripped length from the total specimen length L . By interpolation of the Nicalon strength data presented in Ref. 24, the failure strain of the NLM202 fiber at a 60-mm gauge length is estimated at $\sim 1.0\%$. The

difference of approximately 25% between the maximum bridging strain captured by the LRM-probe and the as-received SiC Nicalon fiber strength indicates that fibers in the composite fail following a different pattern than when tested in air, either as monofilaments or in bundles. While the latter fail at statistical positions along the gauge length determined by the fiber-specific surface flaw distribution,^{4,25} the loci of fiber failure in composites appear to concentrate preferably along the debonded interface and not within the crack flanks where deformation is maximum. In this regard, the failure pattern of fibers in composites can be attributed to the interaction between the debonded interface and the surface of the intact/stretching fiber that slides across it, a mechanical friction process that increases the fiber fatality along the debond region.

The above remark does not imply that the strength of a fiber in a composite material is less than the fiber's strength in air, but stresses that fibers fail due to different reasons in a composite material that they do in air. Additionally, it should not be overlooked that fibers in a composite material are expected to have undergone extensive handling during composite fabrication and to have received severe thermal treatments during composite processing/curing. Such processes certainly affect the integrity, crystallinity, and load bearing capacity of the fibers.

The plateau values of the regressions to the directly-measured bridging strain profiles (Fig. 6) are multiplied by the Young's modulus of the fibers (as in Table I) to provide the LRM stress. These local bridging stresses are compared to the macromechanically derived values of nominal composite stress in Table III. The latter values were obtained for each specimen from the y axis of Fig. 4 ("nominal bridging stress") as the ordinates corresponding to each LRM-AS.

The local and nominal bridging stress behavior of the composite is compared schematically in Fig. 9, where an inverse relation between the two is observed. This

TABLE III. Comparison of directly measured fiber stress with macromechanically established values.

Acquisition stage	Bridging strain (%)		Bridging stress (MPa)	
	Local (LRM)		Local (LRM)	Nominal
Specimen A				
A1	0.117 ± 0.059		258.4 ± 131.2	131
A2	0.713 ± 0.107		1569.9 ± 236.4	77
A3	0.786 ± 0.116		1730.0 ± 256.3	32
Specimen B				
B1	0.118 ± 0.071		261.5 ± 157.6	134
B2	0.242 ± 0.094		533.5 ± 208.5	98
B3	0.680 ± 0.131		1496.6 ± 289.0	66
B4	0.754 ± 0.159		1660.0 ± 351.6	34
Specimen C				
C1	0.267 ± 0.042		587.9 ± 93.9	139

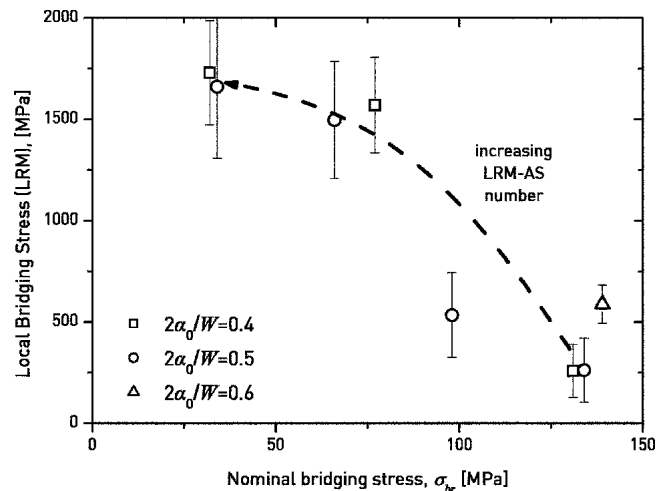


FIG. 9. Comparison of nominal and local bridging stress with different notch lengths.

behavior can be attributed to the fact that fibers probed individually through LRM deform up to failure in a linear-elastic fashion subject to monotonically increasing deformation, load, and stress. In contrast, the macromechanical analysis does not take into consideration the decrease in intact fiber population due to successive fiber failure and assumes a constant bridging zone cross sectional area throughout fracture, equal in value to the initial, stress-free case. The LRM technique, however, can distinguish between fibers that are (i) stress-free due to failure within the crack flanks or complete pull-out, (ii) partially loaded due to incomplete pullout and, finally, (iii) fully loaded. It is worth noting here that LRM cannot distinguish whether the embedded part of a bridging fiber is intact or is undergoing pullout. In the future, similar experiments will be performed on transparent or semi-transparent matrices to observe closely the interfacial micromechanics of these systems.

D. Interfacial-shear strength

It is well known that, following a simple force balance around a failed fiber undergoing pull-out, the interfacial-shear strength τ can be calculated from the fiber strain ϵ as:

$$\tau = \frac{\epsilon E_f r_f}{2l_p}, \quad (4)$$

where r_f is the fiber radius, E_f is the elastic modulus of the fibers, and l_p is the pull-out length. For the composite under investigation, the pull-out length is a statistical parameter varying around the mean value of 690 μm with a standard deviation of 20 μm .¹² The small value of the relevant coefficient of variation, 2%, implies that the assumption of a constant mean pull-out length for all fibers is valid.

Using the values of $E_f = 200 \text{ GPa}$,²⁶ $r_f = 6.5 \mu\text{m}$,²⁴

$l_p = 0.69$ mm, and the plateau value of LRM-measured fiber strain $\epsilon = 0.75\%$, an interfacial-shear strength of 7 MPa is calculated. This value is within the 1–8 MPa range (depending on the radius of the SiC fibers²⁷) of the experimentally measured values of τ for the specific composite. It is also very close to the ISS value of 5.5 MPa²⁶ calculated through the Avenston-Cooper-Kelly model.²⁸ Thus, the directly measured bridging strain values obtained via the LRM technique can also be used in assessing the interfacial shear strength of the composite.

V. CONCLUSIONS

Bridging strain distribution profiles, obtained by in situ LRM-probing of a large number of individual fibers across the bridged ligaments of a notched SiC-fiber reinforced glass-ceramic matrix composite provided important information regarding the fracture behavior of the material. The nominal bridging law of the composite, obtained through a macromechanical elastic displacement correction procedure, indicated a notch-insensitive material fracture. The observation was also supported by the range of effect of strain magnification gradients developing symmetrically in both notch roots that remained constant, in values normalized with respect to ligament width, and among specimens of different notch lengths. The strain was distributed uniformly in the central 0.1–0.9 normalized position across the bridged ligament of the material with the variation in fiber-to-fiber values being characteristic of the statistical nature of fiber failure in composites. Local bridging strain exhibited an increasing behavior within the fiber failure regime while a plateau was noted on the onset of pull-out dominated behavior. The behavior is dependent upon the different nature of the two mechanisms, axial deformation on intact fibers being directly related to increasing composite strain as opposed to friction-confined crack opening during pull-out. The mechanism controlling fiber failure in the composite was identified as fiber-interface interactions increasing the fatality of surface flaw distribution of the fibers.

ACKNOWLEDGMENTS

The authors wish to thank the European Social Fund (ESF), Operational Program for Educational and Vocational Training II (EPEAEK II), and particularly the Program PYTHAGORAS for funding the above work.

REFERENCES

1. B.N. Cox: Extrinsic factors in the mechanics of bridged cracks. *Acta Mater.* **39**, 1189 (1991).
2. R.M.L. Foote, Y-W. Mai, and B. Cotterell: Crack growth resistance in strain-softening materials. *J. Mech. Phys. Solids.* **34**, 593 (1986).
3. T.K. Jacobsen and B.F. Sorensen: Mode I intra-laminar crack growth in composites—modelling of R-curves from measured bridging laws. *Compos. Part A-Appl. S.* **32**, 1 (2001).
4. M. Sutcu: Weibull statistics applied to fiber failure in ceramic composites and work of fracture. *Acta Mater.* **37**, 651 (1989).
5. J. Llorca and N. Singh: Influence of fiber and interfacial properties on fracture behaviour of fiber-reinforced ceramic composites. *J. Am. Ceram. Soc.* **74**, 2882 (1991).
6. F. Zok, O. Sbaizero, C. Hom, and A.G. Evans: Mode I fracture resistance of a laminated fiber-reinforced ceramic. *J. Am. Ceram. Soc.* **74**, 187 (1991).
7. T. Fett, D. Munz, C-T. Yu, and A. Kobayashi: Determination of bridging stresses in reinforced Al_2O_3 . *J. Am. Ceram. Soc.* **77**, 3267 (1994).
8. G. Rausch, M. Kuntz, and G. Grathwohl: Determination of the in situ fiber strength in ceramic-matrix composites from crack-resistance evaluation using single-edge notched-beam tests. *J. Am. Ceram. Soc.* **83**, 2762 (2000).
9. G. Pezzotti, N. Muraki, N. Maeda, K. Satou, and T. Nishida: In situ measurement of bridging stresses in toughened silicon nitride using raman microprobe spectroscopy. *J. Am. Ceram. Soc.* **82**, 1249 (1999).
10. J.D. Belnap, J-F. Tsai, and D.K. Shetty: Direct measurement of crack shielding in ceramics by the application of laser Raman spectroscopy. *J. Mater. Res.* **9**, 3183 (1994).
11. G. Pezzotti, H. Okudaa, N. Muraki, and T. Nishida: In-situ determination of bridging stresses in Al_2O_3/Al_2O_3 -platelet composites by fluorescence spectroscopy. *J. Eur. Ceram. Soc.* **19**, 601 (1999).
12. K.G. Dassios, C. Galiotis, V. Kostopoulos, and M. Steen: Direct in situ measurements of bridging stresses in CFCCs. *Acta Mater.* **51**, 5359 (2003).
13. C. Galiotis, A. Paipetis, and C. Vlattas: Remote laser raman microscopy (ReRaM): Part 1. Design and testing of a confocal microprobe. *J. Raman Spectrosc.* **27**, 519 (1996).
14. C. Galiotis: Interfacial studies on model composites using laser raman spectroscopy. *Compos. Sci. Technol.* **42**, 125 (1991).
15. F. Bollet, C. Galiotis, and M.J. Reece: Measurement of strain distribution in fiber reinforced ceramic matrix composites. *Composites* **27**, 729 (1996).
16. C. Filiou and C. Galiotis: In situ monitoring of the fiber strain distribution in carbon fibre thermoplastic composites using laser raman spectroscopy: Part 1. Effect of applied tensile stress. *Compos. Sci. Technol.* **59**, 2149 (1999).
17. K.G. Dassios and C. Galiotis: Fluorescence studies of polycrystalline Al_2O_3 composite constituents: Piezo-spectroscopic calibration and applications. *Appl. Phys. A* **79**, 647 (2004).
18. L.S. Schadler and C. Galiotis: A review of the fundamentals and applications of LRS microprobe strain measurements. *Int. Mater. Rev.* **40**, 116 (1995).
19. P. Le Coustoumer, M. Monthieux, and A. Oberlin: Understanding Nicalon fiber. *J. Eur. Ceram. Soc.* **11**, 95 (1993).
20. L. Porte and A. Sartre: Evidence for a silicon oxycarbide phase in the Nicalon silicon carbide fiber. *J. Mater. Sci.* **24**, 271 (1989).
21. R.J. Young, A.B.L. Broadbridge, and C-L. So: Analysis of SiC fibers and composites using Raman microscopy. *J. Microsc.* **196**, 257 (1999).
22. N. Melanitis: An investigation of the tensile, compressive and interfacial properties of carbon fibres using laser Raman spectroscopy. Ph.D. Thesis, Queen Mary and Westfield College, University of London, London, UK (1991).
23. G. Anagnostopoulos, J. Parthenios, A.G. Andreopoulos, and

- C. Galiotis: An experimental and theoretical study of the stress transfer problem in fibrous composites. *Acta Mater.* **53**, 4173 (2005).
24. G. Simon and A.R. Bunsell: Mechanical and structural characterization of the Nicalon silicon carbide fiber. *J. Mater. Sci.* **19**, 3649 (1984).
25. W.A. Curtin: Theory of mechanical properties of ceramic-matrix composites. *J. Am. Ceram. Soc.* **74**, 2837 (1991).
26. M. Drissi-Habti: Assessment of the mechanical behavior of SiC fiber reinforced magnesium lithium aluminosilicate glass-ceramic matrix composite tested under uniaxial tensile loading. *J. Eur. Ceram. Soc.* **17**, 33 (1997).
27. M. Benoit, P. Brenet, and D. Rouby: Behavior of interfaces in ceramic-ceramic composites. *Rev. Compos. Mater. Avancés.* **3**, 235 (1993).
28. J. Avenston, G.A. Cooper, and A. Kelly: Single and multiple fracture in the properties of fiber-composites, in *Proceedings of the National Physical Laboratory* (IPC Science and Technology Press Ltd., London, UK, 1971), pp. 15–26.